Design and Performance of the ARIANNA HRA-3 Neutrino Detector Systems

S. W. Barwick, E. C. Berg, D. Z. Besson, T. Duffin, J. C. Hanson, S. R. Klein, S. A. Kleinfelder, *Senior Member, IEEE*, K. Ratzlaff, C. Reed, M. Roumi, T. Stezelberger, J. Tatar, J. Walker, R. Young, and L. Zou

***Abstract*—We report on the development, installation, and operation of the first three of seven stations deployed at the ARIANNA site's pilot Hexagonal Radio Array (HRA) in Antarctica. The primary goal of the ARIANNA project is to observe ultrahigh energy ($>$ 100 PeV) cosmogenic neutrino signatures using a large array of autonomous stations, each 1 km apart on the surface of the Ross Ice Shelf. Sensing radio emissions of 100 MHz to 1 GHz, each station in the array contains RF antennas, amplifiers, 1.92 G-sample/s, 850 MHz bandwidth signal acquisition circuitry, pattern-matching trigger capabilities, an embedded CPU, 32 GB of solid-state data storage, and long-distance wireless and satellite communications. Power is provided by the sun and buffered in $LiFePO_4$ storage batteries, and each station consumes an average of 7 W of power. Operation on solar power has resulted in $\geq$58% per calendar-year live-time. The station's pattern-trigger capabilities reduce the trigger rates to a few milli-Hertz with 4-sigma voltage thresholds while retaining good stability and high efficiency for neutrino signals. The timing resolution of the station has been found to be 0.049 ns, RMS, and the angular precision of event reconstructions of signals bounced off of the sea–ice interface of the Ross Ice Shelf ranged from 0.14 to 0.17°.**

***Index Terms*—Analog integrated circuits, Antarctica, antenna arrays, astrophysics, embedded software, ice shelf, mesh networks, programmable logic arrays, switched capacitor circuits.**

I. Introduction

THE Antarctic Ross Ice-shelf ANtenna Neutrino Array (ARIANNA) project is a surface array of radio receivers planned to span ~1000 km^2 of the Ross Ice Shelf in Antarctica, viewing ~0.5 Teratons of ice [1]–[4]. The project will detect radio waves originating from high energy neutrino interactions with atoms in the ice via the Askaryan Effect [5]. Neutrino interactions produce a shower of secondary particles, plus, for ν_μ charged current interactions, an energetic muon. The secondary particles produce an electromagnetic or hadronic shower which extends over a length of many meters increasing logarithmically with energy, with a transverse dimension of about 10 cm. For wavelengths much larger than this transverse dimension, electromagnetic radiation is coherent, and thus depends on the net charge in the shower. Compton scattering of atomic electrons, and annihilation of shower positrons on atomic electrons both contribute to a net negative charge in the shower, leading to an intense Cherenkov radiation pulse, with a peak electric field that scales linearly with the shower energy. The frequency range of the radiation depends on the angle of observation of the shower. In ice, near the Cherenkov angle of about 56 degrees, the coherent radiation extends up to a maximum frequency of about 1 GHz; away from the Cherenkov angle, the cutoff is lower. ARIANNA is designed to improve the sensitivity to neutrinos with energies in excess of 10^{17} eV by at least an order of magnitude relative to existing limits [6], [7]. Its goals include a confirmation and measurement of the Greisen–Zatsepin–Kuzmin neutrino flux [8], [9], which results from cosmic rays interacting with the diffuse cosmic microwave background, and to measure the neutrino-nucleon cross-section.

ARIANNA takes advantage of unique geophysical features of the Ross Ice Shelf [10], [11]. At ARIANNA's location on the ice shelf, approximately 78.7°S, 165°E, the water–ice interface of the ice shelf acts as a nearly perfect mirror for radio pulses generated by extremely high-energy neutrinos traveling downward and interacting in the interface [12]. The ice's long attenuation length allows for the detection of direct and reflected radio pulses at the surface, far from the interaction point. This and the ice shelf's relative proximity to McMurdo Station (~100 km away) significantly simplifies the deployment of a large array. Moreover, by its uninhabited location, the site has been found to be essentially free of anthropogenic noise.

ARIANNA stations are easy to deploy, maintain, and upgrade. Each station (see Fig. 1) contains RF antennas, amplifiers, triggering, digitization, computing, power management, data storage, long-distance wireless networking and satellite communications, solar power and battery backup, plus experimental wind power. Four stations have been installed, including an early prototype deployed in 2011 [4] and three pilot stations from the pilot seven-station Hexagonal Radio Array (HRA),

Manuscript received March 03, 2015; revised June 30, 2015; accepted July 28, 2015. Date of publication September 29, 2015; date of current version October 09, 2015. This work was supported by funding from the Office of Polar Programs and the Physics Division of the U.S. National Science Foundation, including via grant awards ANT-08339133, NSF-0970175, and NSF-1126672. *(Corresponding author: S. A. Kleinfelder.)*

S. W. Barwick, E. C. Berg, T. Duffin, C. Reed, and J. Walker are with the Department of Physics and Astronomy, University of California, Irvine, Irvine, CA 92697 USA.

S. A. Kleinfelder, M. Roumi, and L. Zou are with the Department of Electrical Engineering and Computer Science, University of California, Irvine, Irvine, CA 92697 USA (e-mail: stuartk@uci.edu).

D. Z. Besson and J. C. Hanson is with the Department of Physics and Astronomy, University of Kansas, Lawrence, KS 66045 USA, and the Moscow Engineering Physics Institute, Moscow, Russia.

S. R. Klein, T. Stezelberger, and J. Tatar are with the Lawrence Berkeley National Laboratory, Berkeley, CA 94720 USA.

K. Ratzlaff and R. Young are with the Instrumentation Design Laboratory, University of Kansas, Lawrence, KS 66045 USA.

Color versions of one or more of the figures in this paper are available online at http://ieeexplore.ieee.org.

Digital Object Identifier 10.1109/TNS.2015.2468182

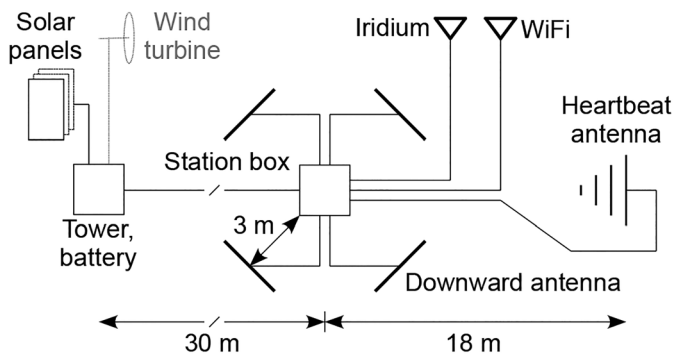

Fig. 1. Schematic station overview showing basic elements and distances (not to scale) of an ARIANNA Hexagonal Radio Array station.

which were deployed in December of 2012 and are the subject of this paper.

ARIANNA is a surface array, with most components buried less than 1 m beneath the snow surface. This design has many practical advantages when compared with deep-ice experiments [13]–[17], the most obvious of which is that no drilling is necessary to deploy the stations, saving an enormous amount of fuel, environmental impact, expense, effort and time. Surface deployment imposes far fewer geometric constraints on receiver antennas and electronic systems than deep-ice designs. In particular, the receiving antennas, which are unconstrained by the need to fit within boreholes, can provide much better measurement of the Cherenkov polarization and, therefore, the event geometry. Cabling between antennas and electronics, etc., are also minimized and at the surface. Deployed equipment is fully retrievable, and servicing or upgrades are possible while keeping most of the installed infrastructure intact.

Sections II–VI of this paper focuses on the design of the major subsystems of the stations deployed in 2012 as part of a pilot phase of the ARIANNA project, known as the HRA. Section VII describes the system software for station monitoring and remote control. It also outlines the data collection, transmission and archiving procedures. Section VIII provides a discussion of the operational performance of the power systems, monitoring systems, trigger rates and environmental influences, and evaluation of the data quality.

II. ARIANNA Hexagonal Radio Array

In 2010, the National Science Foundation approved the HRA pilot program of the ARIANNA project, consisting of seven stations dispersed on the ice in a hexagonal grid with 1 km between neighboring stations. The HRA's focus is to develop the technologies needed for a network of autonomous stations that achieve the performance necessary for the physics aims of the full-scale ARIANNA project. Stations must provide their own power, and must allow unattended remote monitoring, data retrieval and control. Operation at temperatures to –30°C or lower, and survival during harsh Antarctic conditions is a necessity. The electronics must be highly-sensitive over a 100–1000 MHz frequency range and perform without creating any radio frequency noise in this spectrum. Stations must be cost-effective and quick to deploy.

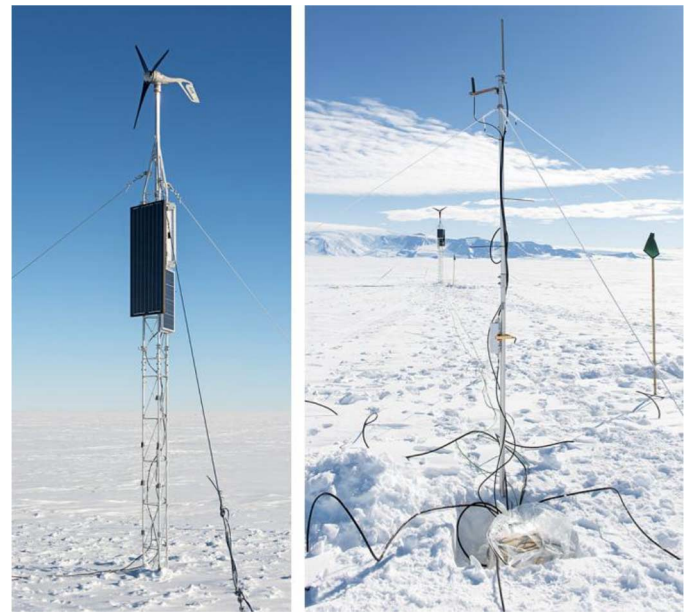

Fig. 2. HRA system on the Ross Ice Shelf during deployment in 2012, showing a power tower (left), a communication's mast (right) with a station box inside clear plastic at the foot of the mast, and a flag marking the location of one of four buried downward-pointing instrumentation antennas.

An early prototype station including a new 1.92 G-samples/s waveform acquisition and advanced real-time triggering system ("ATWD") was deployed in December of 2011 [4]. In December of 2012, ARIANNA deployed the first three HRA stations, and converted the 2011 station to a weather monitoring post and WiFi repeater. The second-generation ARIANNA design replaced the prototype's hand-assembled electronics with a unified, mass-produced printed-circuit electronics system, replaced separate hand-constructed solar panel and wind turbine support structures with an integrated commercial tower system, and made many other refinements resulting in a much lower power ($<$ 7 W average), much lower cost, lighter weight, lower noise, better calibrated and much faster and easier to deploy system.

The National Science Foundation (NSF) approved deployment of the HRA's remaining four stations during the 2014–2015 Austral summer. These stations include simplifications of the power tower, including the integration of the communications antennas, improved amplifiers, and a simpler, lower-cost, lower-power, single board data acquisition system incorporating a new multichannel signal acquisition chip, including deeper waveform storage and simplified trigger formation.

Each ARIANNA HRA station deployed thus far is divided into two major components: a power tower and an instrumentation and communications box with associated antennas. A power tower is shown in Fig. 2 (left), and a communication mast is shown (Fig. 2, right) with an omnidirectional antenna for mesh-connected wireless communications with McMurdo Station via a repeater on Mt. Discovery, plus an antenna for Iridium satellite short-burst messaging.

A station and amplification box assembly (see Sections III and IV) lies at the foot of the communications mast

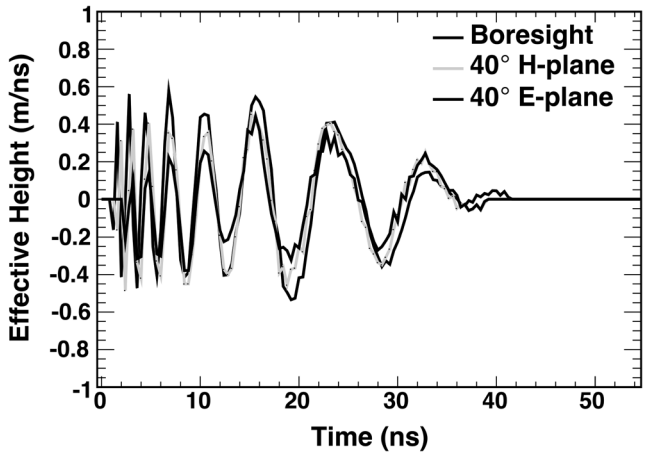

Fig. 3. Example antenna effective height versus off-axis angle for the E- and H-planes at 0° ("boresight") and 40° off-axis.

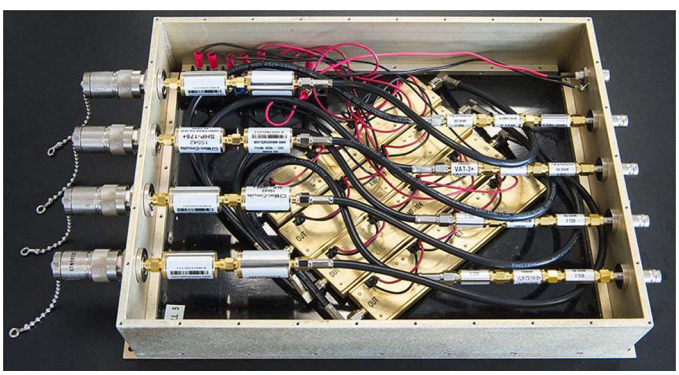

Fig. 4. The 2012 ARIANNA station's amplifier box (inputs to the left, outputs and power to the right). It contains four amplifiers, each with four AC-coupled 1.5 GHz GaAs amplifier stages with interstage bandwidth shaping.

(Fig. 2, right), wrapped in plastic to prevent ice build-up on its connectors, etc. Four signal acquisition antennas surround the communications mast, with the position of one marked by the green flag on the right-hand side of the photo.

III. Antennas and Amplification

Each station includes four log-periodic dipole antennas (Creative Design Co. model CLP5130-2N), positioned as two orthogonal pairs of parallel antennas 6 m apart, pointing straight down into the ice. These antennas have 17 elements and are about 1.4 m long, with the span of its largest tines being 1.45 m. The frequency response ranges from 105–1300 MHz with a VSWR of 2.0:1 or less across the band (in air; in snow, their lower frequency limit is expected to be 70–80 MHz, e.g. in [1]). The forward gain was measured to be 7–8 dBi, with a front-to-back ratio of 15 dB. An example plot of the antenna's measured effective height (ratio of the induced voltage to the incident field) in the E-plane and H-plane at a common 40° off-axis angle is shown in Fig. 3 [18]. The antennas are connected via ~5 m low-loss LMR-400 cable (N-type connectors on both ends) to an RF-tight box containing four radio-frequency amplifiers (Fig. 4). Band-pass filtering leaves a frequency range of 100–1000 MHz intact.

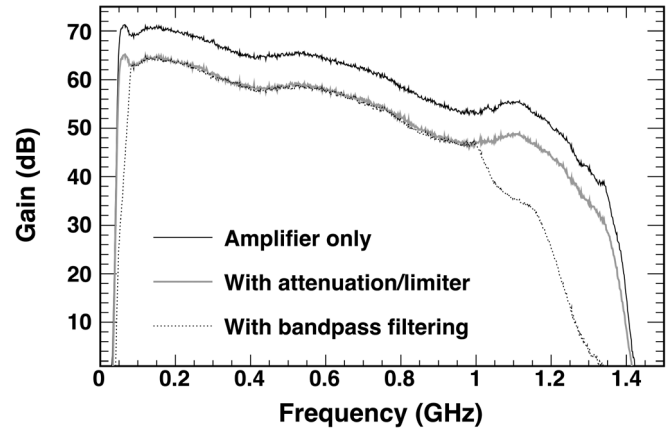

Fig. 5. ARIANNA amplifier gain versus frequency plot. From top to bottom, the curves show the amplifier alone, the amplifier plus output attenuation and limiting, and the former with input band-pass filtering.

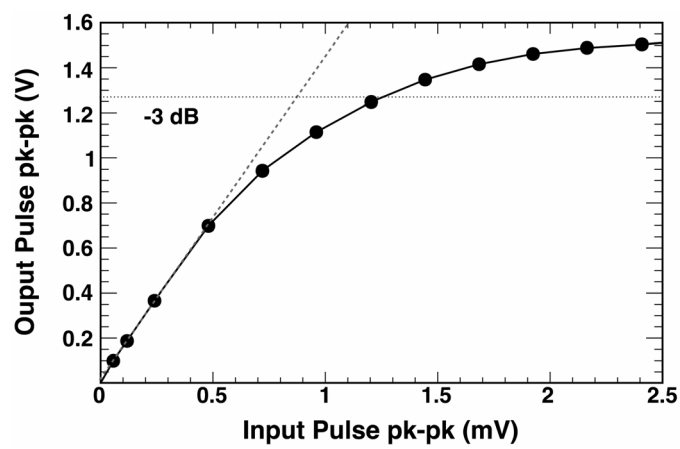

Fig. 6. Amplification system response to an impulsive input signal of varying magnitude, including input band-pass filtering and output limiting and attenuation. Note that the vertical scale is three orders of magnitude greater than the horizontal scale (V versus mV).

Each amplifier consists of four AC-coupled 1.5 GHz GaAs gain stages (Avago MGA-68563) with interstage filtering, yielding about 50–70 dB of gain over the frequency range of interest (Fig. 5). Power is conditioned in the main data acquisition enclosure and is supplied via coaxial cable to the amplifier box. Each amplifier consumes about 250 mW of power at 3.3 V. Amplifiers are housed in individual brass enclosures that help prevent cross-talk between stages and between amplifiers. The amplifier's output range must be matched to the signal sampling and digitization electronics, and hence attenuation and limiting components were added to the amplifier's outputs. The limiting components cause compression of large signals, as shown in Fig. 6, as the departure from linear response for input signals greater than about 0.5 mV.

A. Heartbeat Generation

In order to monitor the health and stability of the ARIANNA stations, each station includes an auxiliary antenna that can transmit a radio-frequency "heartbeat" signal when triggered by the system software. The heartbeat pulse is produced by an FPGA on the system's motherboard, and its width is set in

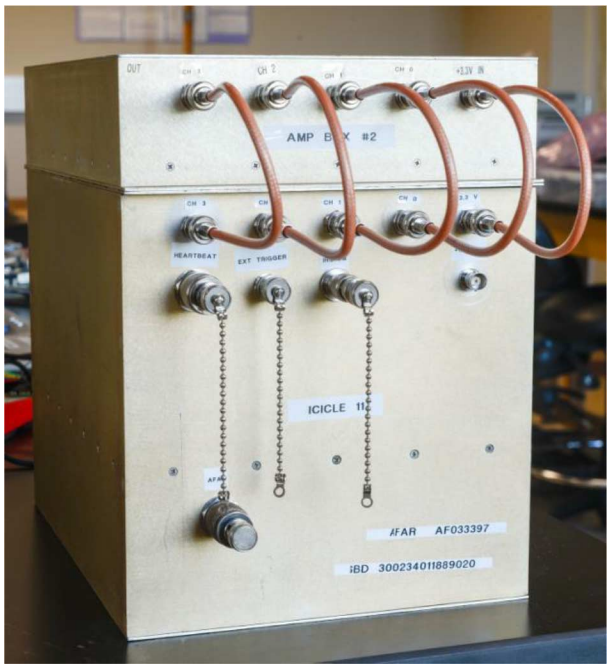

Fig. 7. Example of an HRA station's amplifier box (top portion) and main system box (bottom) containing all data acquisition, control and communications electronics. For scale, the width of the front of the box as shown is 9 in, the depth is 12 in, and the total height is 11.5 in.

firmware to be about 1.5 ns full-width at half-maximum. The resulting signal is sent via LMR 600 cable to the same model log-periodic dipole array antenna as the receiving antennas. The heartbeat antenna is laid ~18 m away from the center of the station with its E-plane parallel to the ground (i.e., flat on the surface), pointing back at the center of the station's antenna array, and aimed approximately along the diagonal between the four instrumentation antennas (i.e., as in Fig. 1).

Heartbeat events are directed to occur on a programmable basis, typically at 1 Hz or less for 5 min every 6 h. The stations trigger-on and record the heartbeat events via their downward-facing receiving antennas, and transmit the digitized waveforms back to the University of California Irvine (UCI) along with other normal events. Heartbeat signals are attenuated such that only the local station can pick them up, and indeed there is no evidence to the contrary. The heartbeat signal verifies correct station operation and detects any short or long-term changes in antenna and amplifier response due temperature or due to any accumulation of snow. As the understanding of this behavior matures, the use of the heartbeat will diminish or cease, and future systems may delete the function entirely.

IV. Data Acquisition System

A new HRA data acquisition system has been prepared and deployed. The main advances of this system are reduced power consumption, greatly improved manufacturability, lower cost, lower noise, improved physical integrity, lighter weight, and more compact dimensions. The overall power consumption has been reduced from ~30 W to $<$ 7 W during typical data taking or communications, with as little as 0.6 W possible in a minimum-power maintenance mode.

Fig. 8. ARIANNA Hexagonal Array data acquisition electronics. It includes four 1.96 GHz data acquisition channels, a 96 MHz 32-bit CPU, communications channels for wireless and satellite short-burst message system, a 32 GB memory card holder for data storage, power conditioning and control for all components, trigger I/O, "heartbeat" pulse generator, etc.

This power reduction maximizes the control, communication and acquisition time during days of waxing and waning sun and/or heavy overcast.

The amplifier and system boxes, as seen in Fig. 7, can be bolted together or kept separate. The amplifier box has four antenna inputs, four amplified outputs, and a 3.3 V power input. The main system box has four amplified signal inputs, 3.3 V power output for the amplifier box, a main power input, a "heartbeat" pulse output, an external trigger input useful during tests, and output ports for Iridium and WiFi communications. The completed station boxes are roughly one cubic foot in size and set up very rapidly in the field.

Fig. 8 shows the 2012 station electronics, consisting of four daughter-cards (one per-channel) and a motherboard (RF amplifiers and the two communications modules not shown). A block diagram of the system is shown in Fig. 9. Each daughter-card contains a 1.92 G-samples/s synchronous switched capacitor array analog sampling and digitization chip (the "ATWD"), a bias-tee module that adapts the dc offset of the incoming signal level to maximize the dynamic range of the ATWD, mode switches, power conditioning, digital-to-analog converters (DACs) for threshold range settings, and a field-programmable gate array (FPGA) that aids in operating the ATWD and allows cards to function as standalone single-channel devices if desired. Although the ATWD chips themselves include 128 ten-bit analog-to-digital converters (ADCs) for fast parallel data conversion, a higher-resolution 12-bit ADC is included on each daughter-card for signal digitization.

The system's motherboard contains all computing, communications interface hardware, data storage and power management circuitry necessary to run the station. It includes power regulation for the antenna amplifiers, a power I/O terminal block, solid-state relays for peripheral power control, voltage and power monitoring circuitry, daughter-card power regulation and control, a holder for a 1.5 Ah lithium battery backup for the real-time clock, a 96 MHz 32-bit ARM Cortex M3 micro-controller, an external trigger input, an FPGA programming port, an Ethernet port used for WiFi communications, an RS-232 port used for Iridium satellite messaging, a 32 GB SDHC flash memory card slot, four daughter-card slots, an FPGA for fast system functions, and the "heartbeat" pulse output.

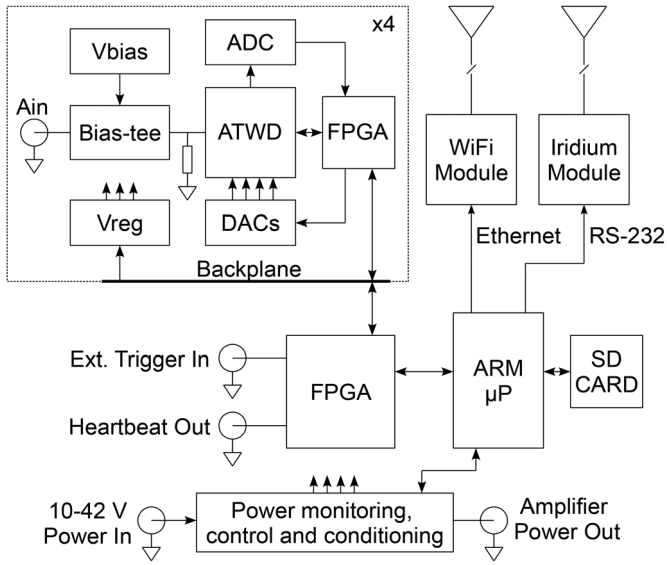

Fig. 9. Simplified block diagram of the ARIANNA system hardware.

V. Waveform Acquisition, Triggering, and Digitization

Triggering and waveform capture is performed by a custom CMOS integrated circuit (Advanced Transient Waveform Digitizer (ATWD) [19]–[22]) running at 1.92 G-samples/s and with ~11.5 bits of dynamic range [23], [24]. A block diagram of the chip's internals is shown in Fig. 10. The chip incorporates real-time pattern-matching trigger functionality that allows, for example, the detection of a bipolar waveform of a certain magnitude and frequency range. A prompt trigger is produced within about 15 ns of the targeted waveform's arrival.

A. Sample Rate and Analog Bandwidth

The ATWD uses a synchronous sample clocking scheme that leads to high sample-to-sample timing uniformity. For convenience, it is driven by a low-speed external clock, which is boosted by a factor of 32 by an on-chip phase-locked loop system and then doubled via interleaving (using both clock phases) by an additional factor of two. The ARIANNA system operates with a 30 MHz reference clock and hence achieves 1.92 G-samples/s operation. By observing a test clock output from the ATWD chips, the timing uniformity of this system has been measured to be ~1 ppm, RMS.

The analog bandwidth of the ATWD sampling and digitization system is an important figure of merit. With a 1.92 GHz nominal sample rate, the Nyquist-limited bandwidth would be 960 MHz, and ARIANNA's amplifiers are low-pass limited to approximately match this frequency. Fig. 11 shows a plot of the frequency response of the data acquisition system as seen in Fig. 8. The frequency response of the entire system (excluding RF amplification) is seen to be flat to under ±1 dB to about 700 MHz, and its −3 dB frequency is about 860 MHz.

B. Trigger Thresholds and Calibration

The ATWD chips perform dual (high and low) threshold triggering in real-time using a unique pattern-searching capability that is applied to the sampled signals rather than the input signal directly. This postsample comparison obviates the need to split the input signal to a separate trigger circuit. It also allows the comparators to be lower in power and slower, yet still, in effect,

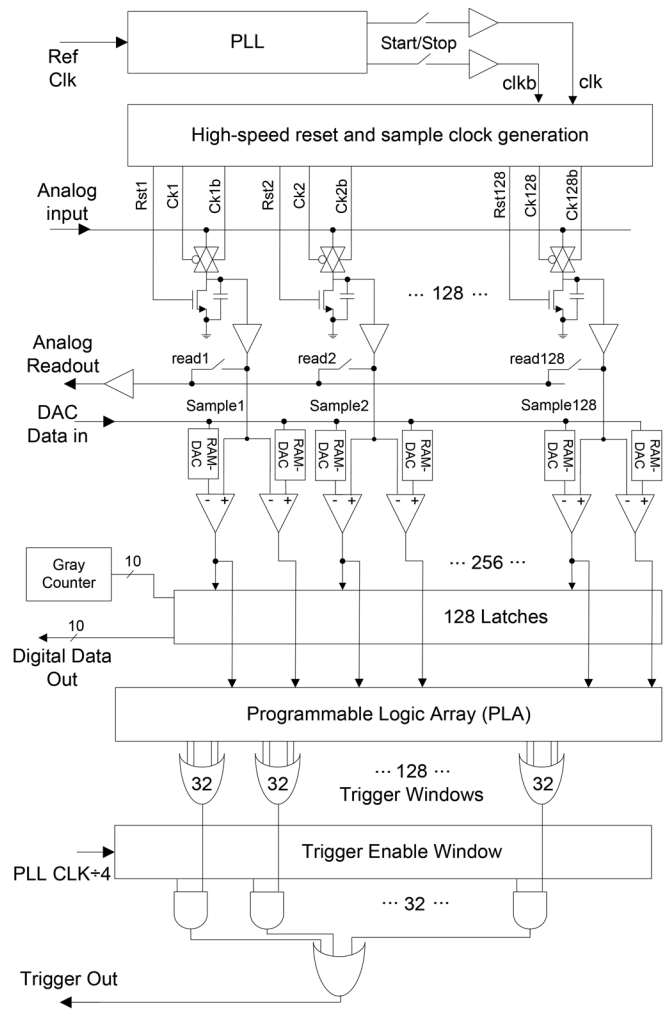

Fig. 10. Block diagram of the 2 G-samples/s synchronous ATWD integrated circuit, showing sampling, comparison, and programmable trigger logic.

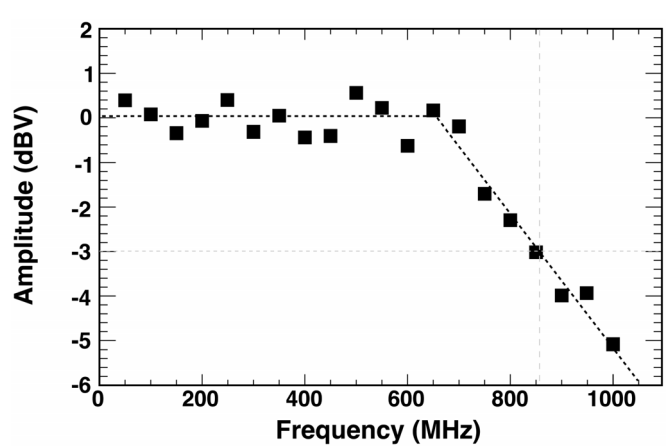

Fig. 11. Data acquisition system bandwidth (excluding amplification), with the slope representing a fit to the higher-frequency data. The bandwidth is flat to under ±1 dB out to ~700 MHz, and the −3 dB bandwidth is ~850 MHz.

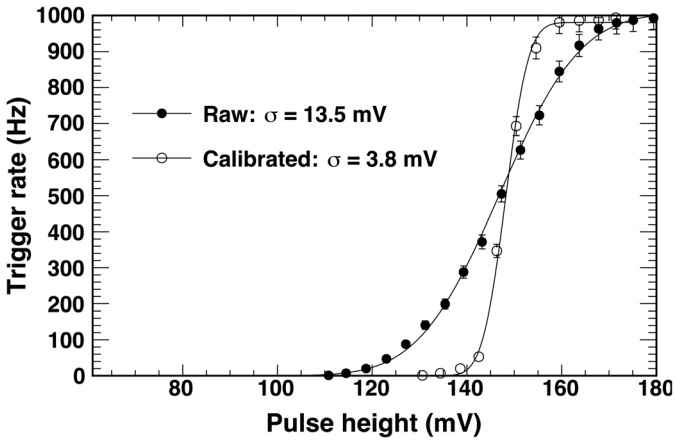

Fig. 12. Example trigger calibration for a single threshold showing trigger rate as a function of pulse height. The curve after calibration shows the variation in thresholds dropping by a factor of 3.6 to a sigma of 3.8 mV.

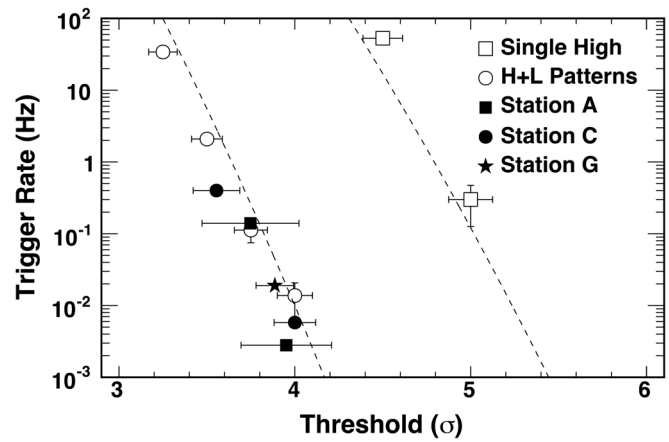

Fig. 13. Laboratory and *in situ* measurements of trigger thresholds versus trigger rates. The "Single High" laboratory measurements represent trigger rates for any crossing above a high threshold. The "H+L Patterns" represent laboratory measurements for an H and L trigger combination coincident within 4 ns. The "Station A, C, and G" data points were from measurements made from three different stations, using the same "H+L Patterns" trigger criteria.

reach the full bandwidth of the ATWD's sampling system (i.e., ~860 MHz).

The basic high and low thresholds are set analogically via external DACs. However, as is the nature of all such electronic circuits, each comparator has a certain random input offset, and hence the ATWD chips include internal digital-to-analog conversion on a per-comparator basis to null these offsets for higher uniformity in triggering performance. To first order, the offsets are a form of "fixed pattern noise" and hence calibrations generally need to be done only once.

Fig. 12 shows an example distribution of the offsets from one set of 128 comparator trigger thresholds (all "high" thresholds of a chip) before and after calibration. The "pulse height" axis represents the magnitude of a unipolar pulse at the channel's ac-coupled analog input that is narrow enough for its peak to be fully contained in one sample. These pulses, produced at 1 kHz, arrive asynchronously with respect to the ATWD's 1.92 GHz sample clock, and hence can arrive at any comparator's sample and hold. With ideal (zero) offsets, the transfer function between pulse height and trigger rate would be a step function from 0 Hz to 1 kHz at a single pulse height. However, in a realistic circuit, differing comparator input offsets lead to curves as seen in the figure. Nulling of these input offsets in this example is found to reduce variation in trigger thresholds from a sigma of 13.5 mV to a sigma of 3.6 mV. The latter number includes the noise of the signal generator itself, and yet is still less than a fifth of the sigma of the amplified thermal output noise from the amplifiers (~22 mV). Since such fixed pattern noise sources are independent and add only in quadrature to thermal noise, variations in trigger thresholds after calibration (in this case) results in only a ~2% net increase over thermal noise in the trigger. The trigger offset nulling DAC values are stored on each daughter-card's FPGA's nonvolatile memory, and are loaded into the ATWDs upon a command to cycle the data acquisition power.

C. Trigger Rate Control

The ATWD has pattern-matching trigger capabilities that aid in trigger rate control [25]. Up to 72 patterns can be loaded into each chip. Each pattern may be a combination of input signal conditions, namely H—the signal must be above a high threshold; L—the signal must be below a separate low threshold; N—neither above nor below (i.e., between the two threshold levels); or X—don't care (does not veto triggers regardless of the signal level). Each pattern consists of eight such conditions, representing eight consecutive samples. A trigger pattern of *HXXXLXXX*, for example, looks for a bipolar signal in which a pair of high and low comparator values are about 2 ns apart (at 1.92 G-samples/s, each sample is 0.52 ns apart).

ARIANNA further employs a second-level trigger that can require a coincidence between a combination of individual channel's triggers, with a programmable level of majority imposed (i.e., 1 or any 2, 3, or all 4 channels coincident within a certain time period). The combination of bipolar trigger patterns, programmable trigger thresholds, and second-level trigger majority logic can flexibly control trigger rates over many orders of magnitude.

Fig. 13 shows laboratory tests of the trigger rate versus threshold while comparing two different patterns, plus *in situ* measurements from the prototype HRA data. The threshold is expressed in terms of the amplifier noise sigma (predominantly amplified thermal noise). The lines represent theoretical estimates of the expected rates. The "Single High" points denote trigger rates when a pattern of *HXXXXXXX* is used. This pattern will trigger on any over-threshold sample and is one of the least restrictive patterns that can be used. The "H+L" patterns trigger on any signal that passes both the high and low thresholds centered over a span of time ranging from 1.56–3.65 ns (based on a 1.92 GHz clock). This set of patterns is more restrictive than the single threshold case yet is efficient for neutrino signatures. The resulting trigger rate drops by over five orders of magnitude for the same threshold values.

The *in situ* measurements are from field data collected after two calibrations made during remote operation in early 2014. These calibrations and measurements were made with the same

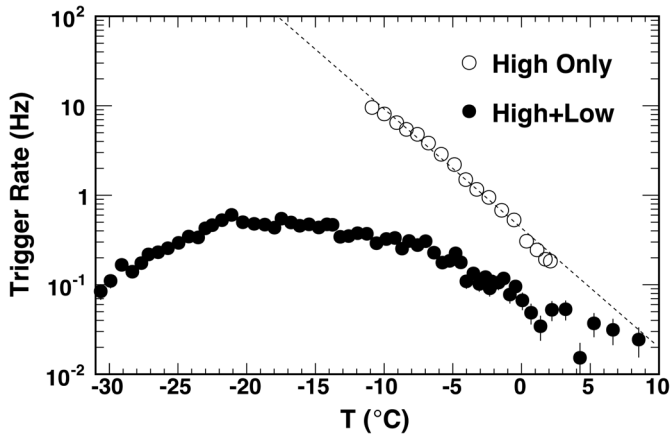

Fig. 14. Thermal trigger rates versus temperature for a single high threshold trigger (open circles), and for a trigger that requires passing a high and a low threshold within 4 ns (filled circles).

five-pattern trigger criteria used in the "H+L" laboratory measurements. Note that all of the data shown in Fig. 13 are also using a "majority-2" criterion, namely that at least two channels must pass the individual channel's trigger criterion within a set period of time (in this case, ~64 ns).

Fig. 14 shows trigger rates in a laboratory test of temperature stability. Two sets of data are shown, one with a High threshold only, and one with an equivalent High and Low coincidence required (over the space of 4 ns). For a single threshold (i.e., High only), a change such as a baseline drift of just a few mV will cause a significant change in trigger rates, and indeed the figure shows about two orders of magnitude change over approximately 15°C, with at least another two orders of magnitude projected down to −30°C (measurements were rate-limited to ~10 Hz, higher than expected *in situ* rates). By contrast, using an equivalent High and Low coincidence results in only one order of magnitude change in trigger rates over the entire expected temperature range once buried in the snow of 0 to –30°C.

A simple automatic threshold monitoring and adjustment system will eventually be put in place in ARIANNA's system software. However, ARIANNA's experience is that remotely performed threshold changes need only be made a few times a year to remain within the system's range of operation and memory capacity. ARIANNA's end goal may be to maintain rates such that all data can be retrieved by Iridium, e.g., rates in the milli-Hz regime, in order to reduce or eliminate any dependence on the high-speed WiFi link, and indeed ~2 MHz rates have been demonstrated in practice.

VI. Power Systems

Given the ARIANNA site's isolation, and the 1 km distance between stations, each station is fully autonomous, including power provision. For the 2012 deployment, the power system for each station consisted of three solar panels, $LiFePO_4$ storage batteries, and experimental use of a wind-turbine.

A. Power Tower and Solar Panels

The HRA stations deployed in 2012 used standard commercially-available radio tower components that were taller and quicker to assemble than the prior custom-made solution, and which integrated both solar and wind power. Each tower was 16 feet in height excluding the wind-turbine extension, and were tied-down by three steel cables connected to wooden anchors buried in the snow. Constructed almost completely of aluminum, the tower assemblies including solar and wind power systems were light enough to be raised manually by one individual.

Solar panels perform well in the Antarctic environment due to the high reflectivity of the snow. For the 2012 deployment, the ARIANNA power towers employed three solar panels mounted in a fixed, vertical, triangular configuration (see Fig. 2, above). A primary 100 W panel was oriented north, and provided more than sufficient power to run the station and maintain a peak battery charging state for nearly as long as the sun remains up. Two secondary 30 W panels were mounted on the other two faces of the triangular tower for supplementary power when the sun is behind the main panel. During the summer, the panels provide enough power that the stations run continuously and exclusively on solar power nearly 100% of the time, even during periods of extensive cloud cover. The panels, being nearly black in color and mounted vertically, have been observed to remain completely free of snow and ice during summer months. Antarctica is exceedingly dry, and indeed no significant snow or ice accumulation has been observed on any above-ice hardware, though drifting snow can accumulate at the surface.

B. Batteries at Cold Temperatures

The pilot ARIANNA stations included batteries to store power for use during overcast days and weeks while the sun is rising and setting. $LiFePO_4$ batteries were selected based on this technology's high physical and chemical stability and safety, and after ARIANNA's experimental tests of performance at cold temperatures. Each of the 3 HRA stations deployed thus far incorporated 2 $LiFePO_4$ batteries of 112 Ah nominal capacity when rated at room temperature (224 Ah total). These were configured in an automobile starting-battery form-factor (Braille Battery Co. model OSGC-12112iB). The batteries include integrated charge controllers which disconnect the batteries when fully charged (e.g., during summer when solar power is plentiful) and when the batteries are nearly depleted, to prevent damage from over-charging and over-discharging.

ARIANNA conducted laboratory tests at −30°C (previously measured to be the lowest expected winter temperature when buried in the snow) and demonstrated that the selected batteries retained about 70% of their nominal storage capacity when charged and discharged at these temperatures. At –30°C, they were capable of accepting a charging current of at least 7A (ARIANNA's expected maximum), and easily provided the expected maximum discharge current consumed by the station electronics of 1A. Fig. 15 displays an example charging and discharging profile of a single 112 Ah (nominal) battery at −30°C. Starting from empty and at −30°C, it required ~89 Ah of charge to reach a full state, at which point the charge controller disconnected the battery. From this state, discharged at 1 A, the battery delivered ~79 Ah of charge until it disconnected. Minor discontinuities in terminal voltages were seen at some points during transitions between a normal and cautionary state indicated by an LED on the battery housing that is driven

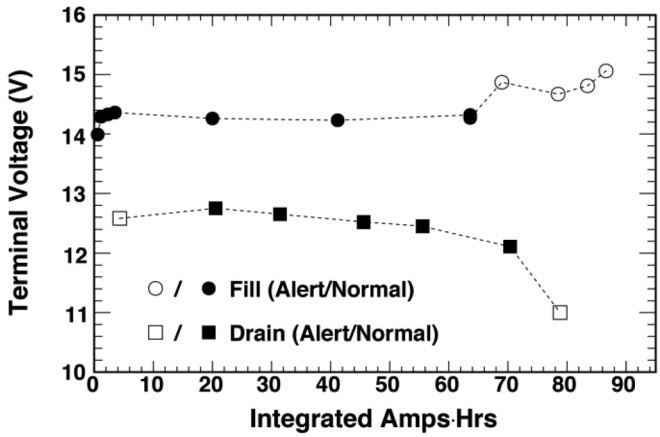

Fig. 15. Terminal voltage of a single battery charging at 7 A and discharging at 1 A, both at $-30°$C. The "alert" versus "normal" measurements denote when an LED on the battery housing indicated a nearly full or nearly empty status.

by the battery's internal charge controller, presumably due to internal switching or rebalancing of cells. Using ARIANNA's expected "worst case" usage profile, these results indicate a useful storage capacity of ~70% of one battery's nominal rating at $-30°$C, and an efficiency of ~89%. The net power available from two batteries stored, charged and discharged at $-30°$C is thus at least 158 Ah, or enough to run the station by itself at full power for at least one week, and for up to one month in a low-duty-cycle power-savings mode.

The batteries for the ARIANNA stations as deployed were contained in insulated enclosures, and all connections between the power tower, the battery box, and the station box were via bayonet connectors and hence were very fast and easy to complete while wearing gloves in the field.

C. Wind Power

Even at < 7 W average power consumption, it has not been considered practical to power the stations by battery alone during the winter. Therefore, ARIANNA has experimented with a number of wind turbines. For the 2012 Austral summer deployment, each of the four stations (the three HRA stations plus the earlier prototype) were equipped with 150 W maximum wind turbines (Southwest Windpower—now Primus Wind Power—model Air 40). As a precaution, the turbines were disassembled and their bearings re-packed with aircraft-grade grease rated to -70C. The Air-40 model uses glass-reinforced nylon blades which, in all stations, survived a year of operation without any issues. Unfortunately, the body of one turbine split open near its mounting collar (apparently a single casting of aluminum or aluminum alloy), leaving it unbalanced and unable to transmit power. A second turbine failed when a bearing burned and seized. Evidence points to both of these failures occurring during a single powerful storm. The third and fourth wind turbines remained intact and fully functional.

During the 2013 servicing mission, the wind turbines were removed from the three 2012 HRA stations, which have henceforth operated on solar power and batteries only. The 2011 prototype station maintained its turbine for continued experimental use, and was reconfigured as an environmental

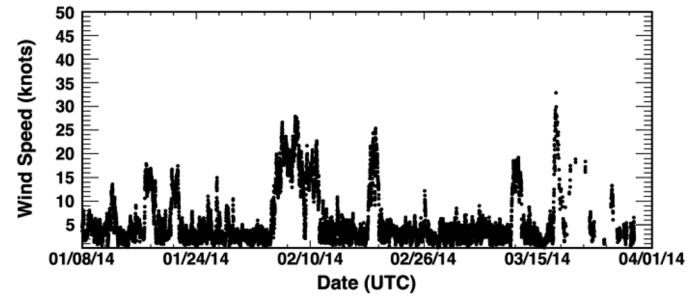

Fig. 16. Wind speed versus time from the 2011 prototype station's anemometer.

monitoring station including air speed and temperature measurements. Fig. 16 shows this station's anemometer data. Wind speeds at the ARIANNA site have been found to be sufficient for significant up-time during winter months, motivating continued interest in experimenting with wind power generation.

VII. Monitoring, Control and Data Collection

The HRA stations are designed to operate autonomously, with remote monitoring, control and data collection made possible by two redundant communications modalities–long distance wireless via a repeater located on Mt. Discovery and satellite short-burst messaging. Communications with each of the ARIANNA stations are handled by a custom software suite built in C++ and Python, via computing facilities at UCI. The Python code works with the Twisted framework to handle TCP communications ("WiFi") and email communications (Iridium Short Burst Data messaging) to and from the stations. Multiple stations can and do communicate concurrently.

A. Communications Overview

The long-range wireless system allows fast and efficient retrieval of all station data, as well as control over each station, including the timing and duration of data acquisition and communications windows, control over which major subsystems are powered, and even the capability of loading new software for the stations' microcontrollers. The wireless modules used are AFAR Communications AR-24027E-SA units, operating at 2.4 GHz. For robustness, the station's wireless communications are mesh-connected, in that every station can act as an intermediate for each other. Communications thus takes place through the "best" path, either directly from a station to McMurdo via repeater on Mt. Discovery, or via a different station that has a stronger signal. It has been found that the 2.4 GHz communications frequency, which is well above the station's sensitive range, does not interfere with the station's data acquisition. Therefore, these modules can remain on, acting as bridges for other stations, during normal operation.

As an alternative, each HRA station is equipped with an Iridium satellite short-burst data (SBD) messaging system. This provides functionality similar to that of a mobile-phone's text messaging system, with messages received by the station consisting of 270 bytes and sent messages containing 340 bytes. Although messages are short, they are densely encoded, and every function available by WiFi is available by SBD. The Iridium modules used are by NAL Research Co., model

9602-N. These operate at ~1.6 GHz, which could interfere with local station signal acquisition (though it is far too weak to be detected by neighboring stations). Thus, they are powered on only during communication, when data acquisition is off. Finally, the Iridium receiver is used to synchronize each station's real-time clock to a highly-precise time received from satellites.

B. System Software and Operation

Each HRA station's system software runs on an NXP LPC1768 embedded microcontroller using a 96 MHz ARM Cortex-M3 core with 32 kB of on-chip RAM and 512 kB of on-chip flash memory. Acquired data are stored on a 32 GB Compact Flash memory card, which is spacious enough to hold a year's worth of data or more even at the highest expected rates.

The system software is programmed in C/C++ without the benefits or overhead of a real-time operating system. The software divides system operation into two major modes or "windows," namely communications and data taking. Generally, these alternate; when communicating, data taking is suppressed and powered-down, and during data taking, communications systems are powered down.

Configuration commands sent to a station during a communications window include parameters such as trigger threshold levels, file and event compression parameters, and communications parameters such as timeout values for communications windows in case two-way communications are not established, the time between communications windows (equivalent to the duration of the data-taking windows), and what data to transmit during communications windows.

During data taking windows the system can collect "thermally" triggered events, periodic forced triggers in which the system takes an event unbiased by the trigger circuitry, and "heartbeat" events, in which the station generates an RF pulse itself and collects the resulting event. Data files collected during these windows include unique event numbers, time-stamp information, voltage readings, losslessly compressed ADC values, bits confirming the type of trigger that resulted in the event (e.g., thermal, forced, etc.), and a 32-bit CRC value to aid in confirming data integrity.

The systems include several features intended to enhance robustness, with particular attention to preventing a system from finding itself in some erroneous state whereby it may lose its ability to communicate, etc. These include a hardware-level "watchdog" timer that will reboot the system if the station becomes locked out of normal operation. The system will also completely reboot if it fails to achieve confirmed communications for five communications windows in a row. Furthermore, received control parameters are not allowed to fall outside of reasonable ranges to prevent user errors from accidentally disabling the stations. For example, it is not possible to set both WiFi and Iridium off during communications windows. Finally, it is possible to remotely upload a new software revision to the station, which, if it passes a CRC check, etc., will take control.

Since there are likely to be periods during which power conservation becomes important, it is possible to individually control which of the major peripherals (amplifiers, data acquisition, WiFi, and Iridium SBD) are on or off during the communications and data-taking windows. For example, the lower-power SBD system can be used exclusively when conserving power becomes important. Finally, the systems can be placed in a strict power-savings mode, in which all data taking is powered down, and communications windows can be less frequent, etc. This mode can be entered automatically by a station when the battery voltage drops below a specified value. Hysteresis is implemented with a second value that prevents the station from dropping into and out of this mode too quickly. A very low-power mode gives operators the ability to maintain control when solar or battery power is low.

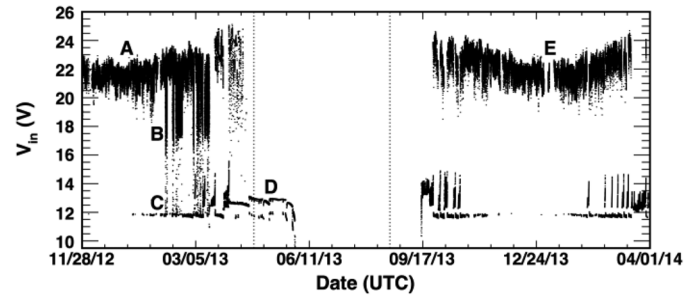

Fig. 17. Example station's power supply voltage versus time. Periods of operation primarily on solar power ("A"), wind power ("B"), battery backup ("C") and solely on battery power ("D") are indicated. Period "E" shows interrupted power during station servicing, and also demonstrates a relationship between seasonal changes and solar power efficiency ("E" was midsummer). The vertical lines indicate the last and first days of sun.

VIII. System Performance

The performance of the first three HRA systems have been extensively studied [26], [27]. This section describes the performance of the power systems, trigger rate performance and stability, noise performance, radio-pulse reflection studies, correlations to neutrino templates, station timing resolution, and event reconstruction resolution.

A. Power Systems Performance

As an example of the power system's performance, Fig. 17 shows voltage readings for an example station ("Site A") during about 14 months of operation, from the time it was turned on in late November 2012 until late December, 2013, when it was disconnected for servicing, and subsequently through March 31, 2014. As evidenced by voltages in the 17–24 V range (regions "A" and "E" in Fig. 17), the solar panels provided nearly all power during the Austral summer. Interestingly, the output voltage of the solar panels climbed during colder months, presumably due to lower levels of recombination and dark current in the solar cells. Battery power is seen supplementing the station's operation in voltage ranges of ~12 to ~14 V (e.g., region "C"). Wind power was observed via voltages between ~14 and ~17 V (region "B") to be frequently and strongly supplementing solar power from early February until mid-March of 2012, when the wind turbine evidently failed during a storm. Beyond this point, solar panels continued to provide significant power, and the batteries were observed to be fully charged during peak daytime hours until mid-April, even when the sun reached only about 2 degrees

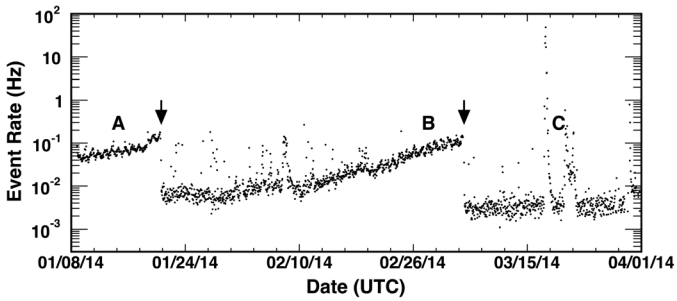

Fig. 18. Total event rates (triggered events only) versus time for Site A from January 8 through March 31, 2014. During periods A and B, slight diurnal rates changes are visible, as is a gradual increase in rates related to a drop in temperature. Two adjustments in rates were made, indicated by the two downward arrows, on or about 1/23 and 3/06. During period C, a powerful storm swept through the area, and an increase in rates was noted.

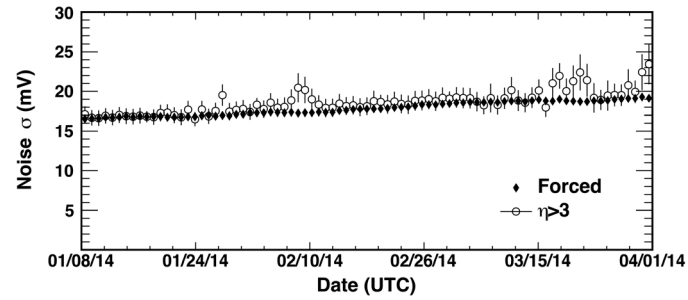

Fig. 19. Noise sigma for channel 2 at Site A between January 8, 2014 and March 31, 2014, binned into one-day periods. The "Forced" data points are unbiased by the system's trigger and reflect highly-Gaussian thermal noise (average of 17.6 mV). The $\eta > 3$ data reflects all data collected due to the station's trigger system except for brief periods or events that include minor amplifier oscillations. Aside from a bias that the trigger imposes, these data are also largely Gaussian, although episodes of greater noise are seen that are correlated with periods of storms including high winds.

maximum height and only about one week before the last sunset on April 24, 2013. After the last sunset (first vertical line in Fig. 17), the station was alternately directed between normal and lower-powered modes in order to prolong testing of the station, e.g. of temperature effects, etc. During this time (region "D"), the station subsisted on battery power only. The station experienced a normal shut-down during while in full data-taking and communications modes on May 30, 2013, 36 days after the last sunset.

The first autonomous communication of the next spring occurred on September 12, 2013, about 3 weeks after the first sunrise (August 19, 2013, indicated by the second vertical line in Fig. 17). This was a day on which the sun had reached a maximum height of 8 degrees. On September 16, 2013, the station began uninterrupted operation until it was serviced in late December 2013. The station thus maintained 256 days of operation out of 365, or 70% of the year including the use of power savings modes. When run at full power continuously, at least 58% live-time over the course of a full year has been achieved.

B. Trigger Rates Versus Temperature and Wind

Fig. 18 shows an example station's ("Site A") thermal-triggered event rate from January 2, 2014 and March 13, 2014. The amplifier's gain has been noted to rise slightly as the temperature drops, leading to increased thermal trigger rates. Once the stations are covered in snow, diurnal temperature changes have been found to be less significant than seasonal changes. Since re-commissioning in January of 2014, the station's thresholds have been remotely adjusted twice, as noted by the two downward arrows in Fig. 19. All stations behaved similarly and required only the same two adjustments.

A partial correlation between storms and/or wind velocity and event rates has been observed. In Fig. 18, the period "C," for example, shows an increase in rates during a storm. The cause and nature of the excess events is being studied, but a few comments can be made: Elevated event rates have been found to be correlated between stations. Generally, only wind speeds above ~20 knots have resulted in elevated event rates, but not all such periods of higher wind speeds have resulted in higher rates. Most of these temporary increases have had negligible impact on event collection efficiency, i.e., less than seasonal temperature variations. No additional noise has been found in forced (unbiased) events during storms, and so there is no evidence that increased trigger rates are due to any gradual, consistent change in the level of noise. Rather, these noise events appeared to be sparse and random. Only one few-hour-long instance (to the left of "C" in Fig. 18) resulted in excess event rates that significantly impacted dead-time. Analysis of the excess triggered events has concluded that they do not resemble expected neutrino events, and that these excess events can be removed from the data with high efficiency, as discussed in the next section.

C. Thermal Noise Measurements

Fig. 19 shows an example plot of recorded noise sigma in mV versus time for a representative data set from 2014 ("Station A," channel 2), binned into one-day intervals. The "Forced" time series consists of all data from "unbiased" events taken at periodic intervals without the involvement of the station's trigger system. These data are highly Gaussian and essentially displays the channel's thermal noise (average $\sigma = 17.6$ mV for all forced triggers). A slight rise in noise versus calendar time is due to the slowly cooling temperatures, which has been found to increase the amplifier's gain and hence the level of recorded noise.

The "$\eta > 3$" time series contains all events acquired via the system's trigger, but excludes those events associated with brief periods in which the station's amplifiers have displayed a sympathetic oscillation between channels (this issue has since been rectified by a revised amplifier design). The parameter "η," detailed in [28], is a count of the number of frequencies containing a large fraction of a waveform's power. A small value of η signifies a single, strong peak at a particular frequency.

The amplitudes measured by each sample in the triggered data are also substantially normally distributed, although amplitudes at the trigger threshold values occur with a higher probability as expected. It is noted that fluctuations in triggered-event noise levels rise modestly above the unbiased event noise levels over the same storm or high-wind periods as seen in Fig. 16 and concomitant with the event rate increases seen in Fig. 18.

D. 2014 Data-Set Correlation Distributions

Data taken between January 8, 2014 and March 31, 2014 have been studied in an exploratory search for neutrino-like

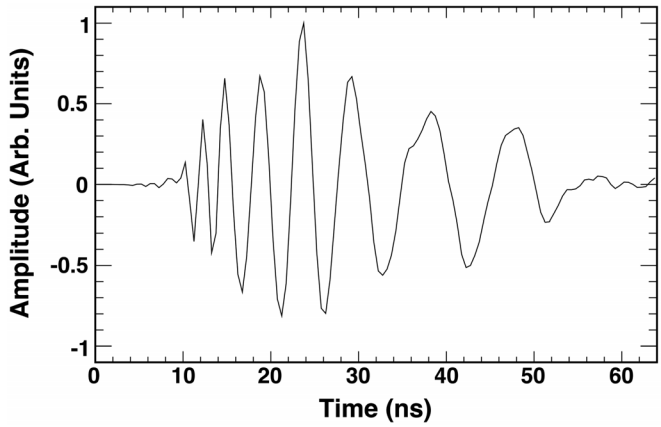

Fig. 20. Example neutrino signal template (40 degrees off-axis in the E-plane) including ice propagation, antenna, amplifier response, but excluding thermal noise, and sampled at 1.92 GHz (Y-axis units are arbitrary).

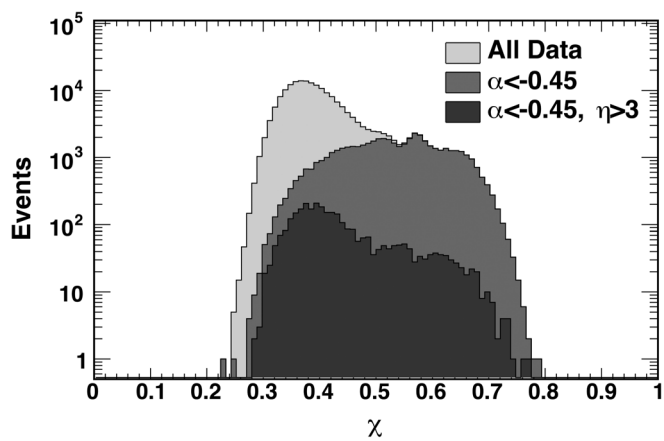

Fig. 21. Distribution of χ in the 2014 data set for Station A, channel 2, for all data, after the $\alpha < -0.45$ cut, and after both the α cut and the "$\eta > 3$" cut.

signals [28]. An expected neutrino signal has been generated from the time dependent electric field at the neutrino interaction vertex, propagated through a model of the ice and convolved with measured antenna and amplifier response functions. The neutrino signals are determined as a function of two space angles defining the orientation of the incident electric field relative to the antenna, as well as the angle between the antenna and the Cherenkov cone. The resulting time dependent neutrino waveform "templates" (e.g., Fig. 20) can then be compared to recorded data by computing its maximum correlation value with each antenna waveform.

Prior to reconstruction of the event direction and polarization, waveforms from all four channels, including both the recorded waveform and its inverse (it is not *a priori* obvious which face of the antenna is presented to the incoming radio wave, hence whether the initial pulse would be positive or negative), for a total of eight waveforms per station, are compared to a single reference template corresponding to 30° in the E- and H-planes. The best correlation between any of these eight signals and the reference template is designated as χ. Fig. 21 shows values of χ in the representative "Site A" data set for all events ("All Data") in its light-gray area, including a total of 203 562 events.

The majority of triggered events are purely random in nature (i.e., thermal noise). These are identified by an autocorrelation function whose results are noted to have a perfect correlation at zero time offset. Nonthermal-noise events are taken to be those for which the minimum autocorrelation function α is below -0.45 on any antenna. These remaining nonthermal events are shown in medium-gray in Fig. 21 ("$\alpha < -0.45$").

The "$\eta > 3$" cut mentioned in the previous subsection is then made in addition to the "$\alpha < -0.45$" cut. This, again, is intended to remove a small subset of events that contain sympathetic amplifier oscillations between channels. To pass this cut, it is required that the frequency spectrum of a neutrino candidate have more than three frequency bins ($\eta > 3$) at or above 50% of the magnitude of the maximum bin—that is, that the candidate contains more than essentially the single-frequency oscillation that is seen in misbehaving amplifiers. Long term, this cut may be unnecessary given demonstrated improvements in amplifier stability. The combination of the α and η cuts is seen in dark gray in Fig. 21. Neutrino candidates are required to pass both the autocorrelation and oscillation cuts, while also correlating well with the expected neutrino signal. The application of the $a < -0.45$, $n > 3$ and chi > 0.81 cuts, described in detail in [28], yields no neutrino candidate events from the data and is found to preserve 90% of simulated neutrino signals.

E. Radio Frequency Reflection Comparisons

Radio-frequency reflection studies on a representative HRA station ("Site G") have been performed. These involved delivering a fast electrical pulse, generated by a Pockels Cell driver (Grant Applied Physics model HYPS) to a quad-ridged polarization horn antenna (Seavey Engineering Inc., now Antenna Research Associates; antenna custom-designed for the ANITA project and described in [29]). The antenna was placed face-down to the ice at various locations both near to and far from the station, as well as oriented in several polarizations relative to the receiving antennas. The transmitted RF pulse therefore passed down through the ice (~550 m thick), bounced off of the water–ice interface, and back up to the station. The station electronics includes an external trigger input that allows the capture of waveforms at precise times, and this was used to trigger the station's data acquisition at the time of arrival of the reflected pulse.

A comparison of reflected waveforms was made between those collected by an ARIANNA station's electronics and equivalent waveforms using same ARIANNA channel's antenna and amplifier but captured by an oscilloscope (Agilent model DSO 7104B; 1 GHz bandwidth, 5 G-samples/s acquisition). As examples, two plots are shown from the same location ("Site G"), with the horn antenna located for a straight down-and-up reflection. It is important to note that the overlapping waveforms shown in these figures are from different transmitted pulses, since it was not possible to record the same reflections at the oscilloscope and station simultaneously while using the same antennas and amplifiers.

The first comparison plot, Fig. 22, shows the station's channel 2's response to the reflected pulse (antenna oriented with parallel polarization to the transmitted pulse) superimposed on an

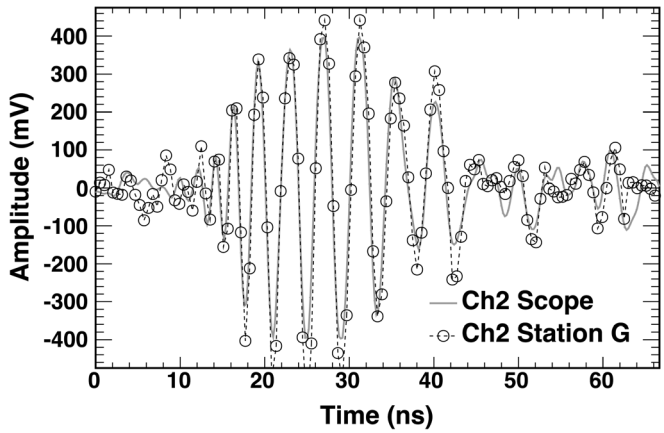

Fig. 22. Overlapping comparison of a representative antenna and amplifier response to separate but equivalent RF pulses reflected off of the bottom of the Ross Ice Shelf, as received by the Station G electronics and by a 1 GHz bandwidth oscilloscope. The polarization of the transmitted pulse was parallel to that of the receiving antenna.

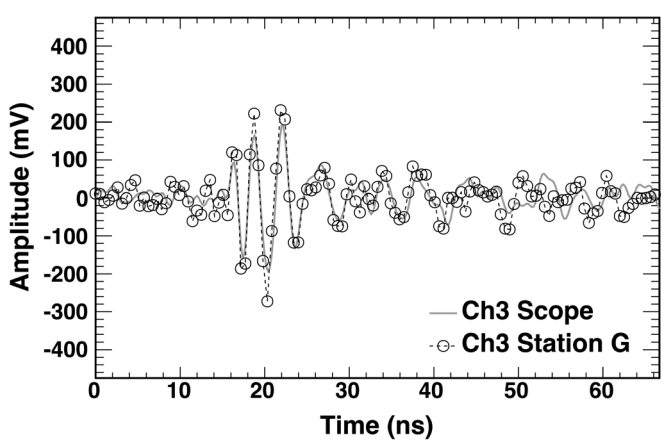

Fig. 23. Overlapping comparison of an antenna and amplifier response to separate but equivalent RF pulses reflected off of the bottom of the Ross Ice Shelf, as in Fig. 22. The polarization of the pulse was orthogonal to the receiving antenna and hence is attenuated.

equivalent pulse's response as recorded by the oscilloscope. Adjustments of the station's response to the vertical scale were made solely according to the station's calibration for gain.

Fig. 23 compares a pulse received at the station's channel 1, whose antenna is orthogonal to that of channel 2 and thus orthogonal to the polarization of the transmitted pulse. Channel 1's response is attenuated compared to channel 2's, consistent with the difference in orientation. The polarization is evidently substantially maintained even after the reflection and transmission through a total of ~1100 m of ice.

It can be seen that the waveforms shown in Figs. 22 and 23 are well-matched within the limits of noise (~22 mV RMS for the amplified thermal noise).

F. Station Timing Resolution

"Site G" reflection studies, performed over a period of 24 h for a variety of surface locations, have been was used to determine the station's timing resolution. For a given surface location, a reference event was arbitrarily selected to generate four Δt_i values, where Δt_i represents the time difference in the

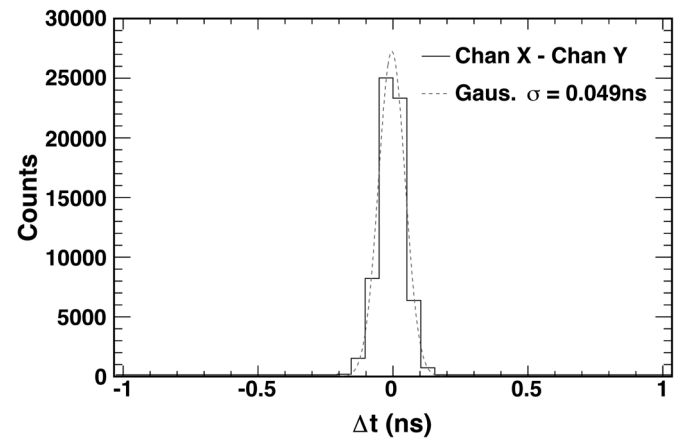

Fig. 24. Measured net timing resolution of the station at Site G, found via reflection studies initiated from a number of locations on the ice. The sigma of a fitted Gaussian is 0.049 ns.

pulse arrival time between channel i in the reference and current event. The time difference is taken to be that which maximizes the Pearson correlation between the waveforms on the ith channel in the reference and current event. This time difference may be nonzero due to jitter in the electronics used to generate the transmission pulse. However, all channels should have the same Δt_i value, since jitter in the pulse transmission time should affect all channels equally. The difference in Δt_i values between channels gives a measure of the readout timing resolution. Fig. 24 shows the time difference $\Delta t = \Delta t_i - \Delta t_j$ for all six combinations of unique channel pairs i and j, integrated over all events taken at all transmission locations. A net timing resolution of 0.049 ns, obtained from a Gaussian fit to the peak, fully satisfies the experimental requirements of ARIANNA.

G. Angular Resolution and Event Reconstruction

Analysis of event reconstruction was performed using data taken in 2012 [30]. In brief, maximum cross-correlations were found between waveforms from all combinations of different channels. This leads to computed time differences between the channels and hence the angle at which a plane-wave is presumed to have struck the different antennas. The reconstructed angle at the station is then corrected for propagation through the firn layer (a layer of compacted snow from prior seasons) with a simple model of ice density as function of depth to produce a predicted signal-source location on the surface of the ice. The median value for the precision of the angular measurements for several different locations ranged between 0.14 to 0.17 degrees, consistent with the measured timing resolution of the data acquisition system, i.e., Fig. 24.

IX. On-Going and Future Effort

The HRA systems have demonstrated that the ARIANNA site is substantially free of anthropogenic noise, achieving ~2 MHz trigger rates at 4-sigma thresholds. Current research is aimed at reducing both thresholds and rates even further by improved triggering configurations, e.g. by requiring higher levels of channel trigger coincidences and with enhanced data processing. In this way, the use of Iridium satellite communications

alone may suffice. Recent efforts have demonstrated that this is achievable using existing remotely-programmable configuration changes. The "WiFi" repeater on Mt. Discovery is a genuine and valued convenience, but it requires maintenance and is a point of potential failure. An Iridium-only solution, by contrast, would make each station completely independent.

Many of the challenges to this project have centered on its remoteness, necessitating autonomous operation, and on the harshness of the environment, including cold temperatures and powerful storms. It has been found that fixed mechanical and electronic systems, whether buried or exposed, including solar panels and satellite communications, have functioned well and reliably. Remote monitoring, control and near-real-time full data transmission by long-distance wireless and satellite, and even the remote updating of the station's system software, have also been reliable.

On the other hand, wind power, at least when using low-cost turbines that have not been ruggedized for Antarctic conditions, has not proven to be mechanically reliable enough given the powerful storms that can occur. Since good up-time has been achieved with solar only, wind turbines have been deleted from the project for the sake of cost and deployment time and effort. This has the side effect of drastically reducing the battery capacity required per station, as quite large batteries are needed to outlast lulls in wind power. Instead, a taller integrated tower containing solar panels and all communications, co-located with the station electronics, will be employed. Without the clearance required for wind-turbines, and using 20-ft towers instead of 16 ft, solar panels and antennas can be mounted higher, extending ARIANNA's operational lifetime in the face of drifting snow.

Similarly, batteries are a perennial concern in Antarctica due to their reduced performance and increased vulnerability at very cold temperatures. Given the transition to a solar power-only mode, it is expected that considerably smaller batteries, sufficient to sustain the stations during days of waxing and waning sun or cloud cover, etc., will be used. These will be enclosed inside the station box seen in Fig. 7, containing any possible electronic noise from their charge controllers and keeping them considerably warmer during operation, hence improving their performance. The deletion of wind turbines and the concomitant reduction in required battery capacity alone saves about 30% of a station's cost. The sum of the above also substantially reduces per-station deployment time, and it eliminates the great majority of a station's risk profile.

Finally, improved amplifiers and a new, very low power (~1.7 W) single-board electronics system, including a new four-channel, 256-sample-per-channel Switched Capacitor Array waveform recording chip, the "SST" [31], have been developed. These were designed for complete drop-in physical and electrical compatibility with the systems described in this paper. The new amplifiers have flatter frequency response and incorporate the filtering and limiting components seen in Fig. 4, reducing costs. The new single-board system electronics similarly reduces that system's expense by approximately a factor of 5, while reducing its power by a factor of 3 and lowering its calibration overhead. The SST chip has equal or higher performance in essentially every respect, including performance and features that significantly improves upon analog bandwidth, trigger sensitivity and ease of calibration.

In early to mid-December of 2014, four new HRA systems using most of the above improvements, including the new amplifiers and the new SST-based data acquisition systems, were successfully deployed. Measurement and evaluation of their design and performance is currently on-going and will be the subject of future publications.

Acknowledgment

The authors wish to thank the staff of Antarctic Support Contractors, Lockheed, and the entire crew at McMurdo Station for excellent logistical support. The authors also thank W. Huang and S.-H W. Chiang for their efforts in the design of the ATWD circuit as discussed in Section V and in [23] and [24]. Lastly, the authors also thank Prof. De Flaviis for the use of the Far Field Anechoic Chamber at the University of California, Irvine.

References

[1] L. Gerhardt *et al.*, "A prototype station for ARIANNA: A detector for cosmic neutrinos," *Nucl. Inst. Meth. A*, vol. 624, no. 1, pp. 85–91, May 2010.

[2] S. W. Barwick for the ARIANNA Collaboration, "ARIANNA–A new concept for high energy neutrino detection," in *Proc. 32nd Int. Cosmic Ray Conf.*. Beijing, China, pp. 238–239, 2011.

[3] S. Klein for the ARIANNA Collaboration, "A radio detector array for cosmic neutrinos on the Ross Ice Shelf," *IEEE Trans. Nucl. Sci.* vol. 60, no. 2, pp. 637–643, Apr. 2013.

[4] S. A. Kleinfelder for the ARIANNA Collaboration, "Design and performance of the autonomous data acquisition system for the ARIANNA high energy neutrino experiment," *IEEE Trans. Nucl. Sci.* vol. 60, no. 2, pp. 612–618, Apr. 2013.

[5] G. A. Askaryan, "Excess negative charge of an electron-photon shower and its coherent radio emission," *J. Exp. Theor. Phys.*, vol. 14, pp. 441–443, Feb. 1962.

[6] K. Dookayka, "Characterizing the search for ultra-high energy neutrinos with the ARIANNA detector," Ph.D. dissertation, Univ. California, Irvine, CA, USA, 2011.

[7] K. Dookayka for the ARIANNA Collaboration, "Characterizing the search for UHE neutrinos with the ARIANNA detector," in *Proc. 32nd Int. Cosmic Ray Conf.*. Beijing, China, 2011.

[8] K. Greisen, "End to the cosmic-ray spectrum?," *Phys. Rev. Lett.*, vol. 16, no. 17, pp. 748–750, Apr. 1966.

[9] G. T. Zatsepin and V. A. Kuzmin, "Upper limit of the spectrum of cosmic rays," *J. Experimental and Theo. Phys. Lett.*, vol. 4, pp. 78–80, 1966.

[10] C. S. Neal, "The dynamics of the Ross ice shelf revealed by radio echo-sounding," *J. Glaciol.*, vol. 24, pp. 295–307, 1979.

[11] S. W. Barwick for the ARIANNA Collaboration, "Performance of the ARIANNA prototype array," in *Proc. Int. Cosmic Ray Conf.*. Rio De Janeiro, Brazil, Jul. 2013.

[12] J. C. Hanson for the ARIANNA Collaboration, "Ross ice shelf thickness, radio-frequency attenuation and reflectivity: Implications for the ARIANNA UHE neutrino detector," in *Proc. Int. Cosmic Ray Conf.*. Beijing, China, 2011.

[13] T. Barrella, S. Barwick, and D. Saltzberg, "Ross ice shelf in situ radio-frequency ice attenuation," *J. Glaciol.*, vol. 57, no. 201, pp. 61–66, Feb. 2011.

[14] E. Andres *et al.*, "The AMANDA neutrino telescope: Principle of operation and first results," *Astropart. Phys.*, vol. 13, no. 1, pp. 1–20, Mar. 2000.

[15] I. Kravchenko *et al.*, "Limits on the ultra-high energy electron neutrino flux from the RICE experiment," *Astropart. Phys.*, vol. 20, no. 2, pp. 195–213, Nov. 2003.

[16] J. Ahrens *et al.*, "Sensitivity of the icecube detector to astrophysical sources of high energy muon neutrinos," *Astropart. Phys.*, vol. 20, no. 5, pp. 507–532, Feb. 2004.

[17] P. Allison *et al.*, "Design and initial performance of the askaryan radio array prototype eev neutrino detector at the south pole," *Astropart. Phys.*, vol. 35, no. 7, pp. 457–477, Feb. 2012.

[18] S. W. Barwick *et al.*, "Time-domain response of the ARIANNA detector," *Astropart. Phys.*, vol. 62, pp. 139–151, Sep. 2014.
[19] S. A. Kleinfelder, "A multi-gigahertz analog transient waveform recorder integrated circuit," Thesis, Univ. California, Berkeley, 1992.
[20] S. A. Kleinfelder, "Advanced transient waveform digitizers," in *Proc. SPIE Particle Astrophysics Instrumentation*, Aug. 2002, vol. 4858, pp. 316–326.
[21] S. A. Kleinfelder, "A multi-GHz, multi-channel transient waveform digitization integrated circuit," in *Proc. IEEE Nuclear Science Symp.*, Orlando, FL, USA, Oct. 2002.
[22] S. A. Kleinfelder, "GHz waveform sampling and digitization circuit design and implementation," *IEEE Trans. Nucl. Sci.*, vol. 50, no. 4, pp. 955–962, Aug. 2003.
[23] W. Huang, S. W. Chiang, and S. Kleinfelder, "Waveform digitization with programmable windowed real-time trigger capability," in *Proc. IEEE Nuclear Science Symp.*, Orlando, FL, USA, Oct. 2009.
[24] S. A. Kleinfelder, S. W. Chiang, and W. Huang, "Multi-GHz waveform sampling and digitization with real-time pattern-matching trigger generation," *IEEE Trans. Nucl. Sci.*, vol. 60, no. 5, pp. 3785–3792, Oct. 2013.
[25] M. Roumi, "Advanced pattern-matching trigger system for the ARIANNA high-energy neutrino detector," Ph.D. dissertation, Univ. California Irvine, Irvine, CA, USA, 2014.
[26] J. Tatar, "Performance of sub-array of ARIANNA detector stations during first year of operation," Ph.D. dissertation, Univ. California Irvine, Irvine, CA, USA, 2013.
[27] J. C. Hanson, "The performance and initial results of the arianna prototype," Ph.D. dissertation, Univ. California Irvine, Irvine, CA, USA, 2013.
[28] S. W. Barwick *et al.*, "A first search for cosmogenic neutrinos with the ARIANNA hexagonal radio array," *Astropart. Phys.*, vol. 70, pp. 12–26, Oct. 2015.
[29] P. Gorham *et al.*, "The Antarctic impulsive transient antenna ultra-high energy neutrino detector (ANITA): Design, performance, and sensitivity for 2006–2007 balloon flight," *Astroparticle Phys.*, vol. 32, pp. 10–41, 2009.
[30] C. Reed for the ARIANNA Collaboration, "Performance of the ARIANNA neutrino telescope station," in *Proc. Int. Cosmic Ray Conf.*. Rio De Janeiro, Brazil, Jul. 2013.
[31] S. A. Kleinfelder, E. Chiem, and T. Prakash, "The SST fully-synchronous multi-GHz analog waveform recorder with Nyquist-rate bandwidth and flexible trigger capabilities," in *IEEE Nuclear Science Symp. Conf. Rec.*, Seattle, WA, Nov. 2014.